The Astrophysical Journal, 759:55 (8pp), 2012 November 1 doi:10.1088/0004-637X/759/1/55

QUADRATURE OBSERVATIONS OF WAVE AND NON-WAVE COMPONENTS AND THEIR DECOUPLING IN AN EXTREME-ULTRAVIOLET WAVE EVENT

Y. Dai[1,2], M. D. Ding[1,2], P. F. Chen[1,2], and J. Zhang[3]
[1] School of Astronomy and Space Science, Nanjing University, Nanjing 210093, China; ydai@nju.edu.cn
[2] Key Laboratory of Modern Astronomy and Astrophysics (Nanjing University), Ministry of Education, Nanjing 210093, China
[3] School of Physics, Astronomy, and Computational Sciences, George Mason University, Fairfax, VA 22030, USA
Received 2012 May 29; accepted 2012 August 22; published 2012 October 17

ABSTRACT

We report quadrature observations of an extreme-ultraviolet (EUV) wave event on 2011 January 27 obtained by the Extreme Ultraviolet Imager on board the *Solar Terrestrial Relations Observatory*, and the Atmospheric Imaging Assembly on board the *Solar Dynamics Observatory*. Two components are revealed in the EUV wave event. A primary front is launched with an initial speed of ∼440 km s^{-1}. It appears that significant emission enhancement occurs in the hotter channel while deep emission reduction occurs in the cooler channel. When the primary front encounters a large coronal loop system and slows down, a secondary, much fainter, front emanates from the primary front with a relatively higher starting speed of ∼550 km s^{-1}. Afterward, the two fronts propagate independently with increasing separation. The primary front finally stops at a magnetic separatrix, while the secondary front travels farther until it fades out. In addition, upon the arrival of the secondary front, transverse oscillations of a prominence are triggered. We suggest that the two components are of different natures. The primary front belongs to a non-wave coronal mass ejection (CME) component, which can be reasonably explained with the field-line stretching model. The multi-temperature behavior may be caused by considerable heating due to nonlinear adiabatic compression on the CME frontal loop. As for the secondary front, it is most likely a linear fast-mode magnetohydrodynamic wave that propagates through a medium of the typical coronal temperature. X-ray and radio data provide us with complementary evidence in support of the above scenario.

Key words: Sun: corona – Sun: coronal mass ejections (CMEs) – Sun: magnetic topology – waves

Online-only material: animations, color figures

1. INTRODUCTION

One of the most intriguing phenomena discovered by the Extreme-ultraviolet (EUV) Imaging Telescope (EIT; Delaboudinière et al. 1995) on board the *Solar and Heliospheric Observatory* (*SOHO*) satellite are "EIT waves," which are characterized by a diffuse bright front globally propagating through the solar corona (Moses et al. 1997; Thompson et al. 1998). EIT waves were initially interpreted as fast-mode magnetohydrodynamic (MHD) waves in the corona (Thompson et al. 1999), which can freely travel across magnetic field lines, covering quite a large fraction of the solar disk. If the coronal fast-mode wave is strong enough, it can also perturb the much denser chromosphere at its base to produce an Hα Moreton wave, just as in the scenario proposed by Uchida (1968). Many subsequent numerical and observational studies (e.g., Wang 2000; Wu et al. 2001; Warmuth et al. 2004; Veronig et al. 2006; Long et al. 2008; Gopalswamy et al. 2009; Patsourakos et al. 2009) have provided further evidence for this view.

This fast-mode wave model was first challenged by Delannée & Aulanier (1999), who found that an EIT wave stopped at the magnetic separatrix, which is difficult to explain in the wave framework. In addition, other case studies have revealed that the EIT wave front is cospatial with the coronal mass ejection (CME) frontal loop (e.g., Attrill et al. 2009; Chen 2009; Dai et al. 2010). Hence, several alternative models have been proposed which consider EIT waves to be a result of magnetic reconfiguration related to the CME liftoff rather than a true wave in the corona. These non-wave models include the current shell model (Delannée 2000), the field-line stretching model (Chen et al. 2002, 2005), and the successive reconnection model (Attrill et al. 2007). Moreover, some other authors claim that EIT waves are a type of slow-mode MHD wave (Wills-Davey et al. 2007; Wang et al. 2009). For more details on the observations and modeling of EIT waves, please refer to the recent literature (Wills-Davey & Attrill 2009; Gallagher & Long 2011; Zhukov 2011; Chen 2011; Patsourakos & Vourlidas 2012).

Chen et al. (2002) predicted that there should be a fast-mode wave ahead of the EIT wave, which was confirmed by Harra & Sterling (2003). On the other hand, Zhukov & Auchère (2004) suggested that from an observational point of view, there could be both wave and non-wave components in an EIT wave. However, early EIT wave studies aiming to pinpoint these components often suffered from a low EIT cadence, which was 12 minutes at best. The situation has been greatly improved with the launch of the *Solar Terrestrial Relations Observatory* (*STEREO*; Kaiser et al. 2008) and the *Solar Dynamics Observatory* (*SDO*; Pesnell et al. 2012). Thanks to the much higher temporal resolution of the EUV telescopes on board the three spacecraft, the multiple components in an EIT wave have been successfully identified in observations (e.g., Liu et al. 2010; Chen & Wu 2011; Cheng et al. 2012; Asai et al. 2012) and verified in calculations (e.g., Cohen et al. 2009; Downs et al. 2011, 2012). With the observations from the modern generation of EUV imagers, we now prefer the more general term "EUV wave" to the conventional "EIT wave." In this paper we report quadrature observations of two components and their decoupling in an EUV wave event on 2011 January 27 from both *STEREO* and *SDO*. The distinct differences in amplitude, kinematics, and multi-temperature behavior imply their different physical mechanisms. In Section 2 we introduce the instruments and data sets. An analysis is carried out and

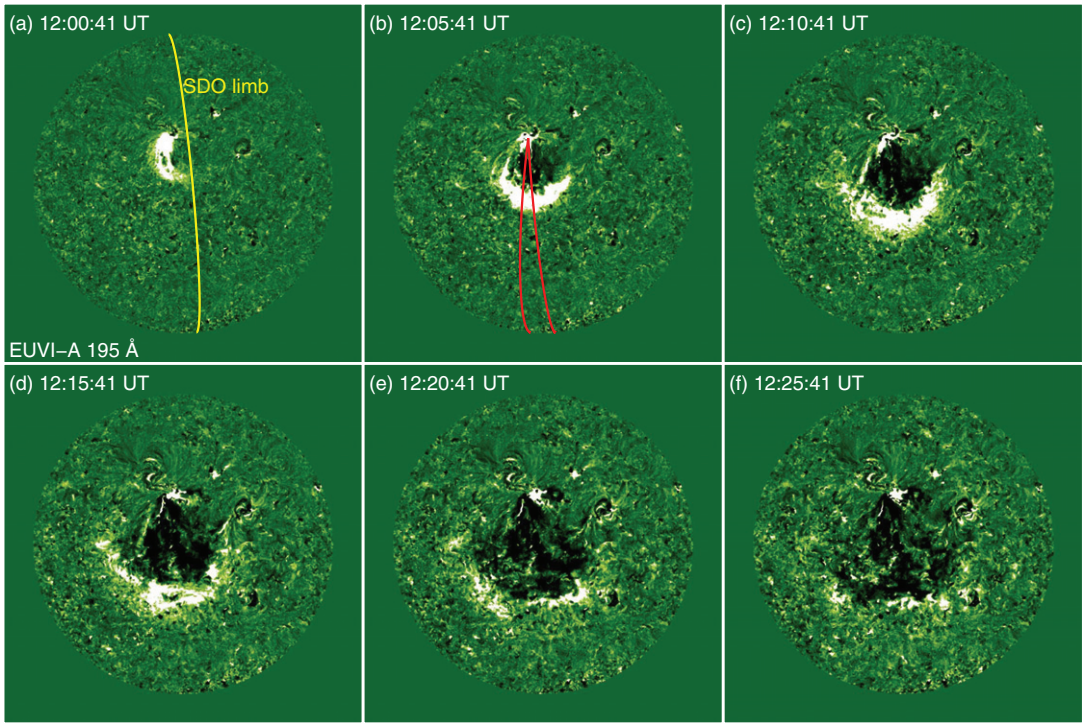

Figure 1. Base ratio images of the EUV wave taken by *STEREO-A*/EUVI at 195 Å. The yellow line outlines the solar limb viewed from *SDO*, and the red lines indicate great circles through the eruption center (−100″, 300″) that border the wave sector in a 180° ± 5° direction within which the wave kinematics are studied. Note that all *STEREO-A* observation times in this work are corrected to Earth UT to compensate for the slight difference in light travel times from the Sun to *STEREO-A* and *SDO*.
(An animation and a color version of this figure are available in the online journal.)

the results are presented in Section 3. We discuss the results in Section 4 and draw our conclusions in Section 5.

2. INSTRUMENTS AND DATA SETS

The EUV wave under study was launched on 2011 January 27 around 12:00 UT from the NOAA active region (AR) 11149, when the AR was very close to the northwest limb from an Earth perspective. At that time, the *STEREO Ahead* satellite (*STEREO-A*) was ∼86° west of the Earth. Therefore, the location of the source region and the quadrature configuration of *STEREO-A* and near-Earth *SDO* offer us a perfect opportunity to trace the evolution of the EUV wave both face-on (from *STEREO-A*) and edge-on (from *SDO*).

We used EUV imaging data from the Extreme Ultraviolet Imager (EUVI; Wuelser et al. 2004) on board *STEREO* and the Atmospheric Imaging Assembly (AIA; Lemen et al. 2012) on board *SDO*. EUVI, part of the SECCHI (Howard et al. 2008) instrument suite, observes the chromosphere and corona up to 1.7 $R_\odot$ in four EUV channels with a pixel size of 1.″58. AIA provides multiple simultaneous images of the transition region and corona up to 1.5 $R_\odot$ in 10 EUV and UV channels with 0.″6 pixel size and 12 s temporal resolution. In this work, we focused on the *STEREO-A*/EUVI (hereafter EUVI-A) 195 Å and AIA 171, 193, and 211 Å observations for the reason that, in general, EUV waves are best observed at these wavelengths (cf. Veronig et al. 2008; Li et al. 2012). During the period of interest the cadence of the EUVI-A 195 Å channel was 5 minutes.

3. ANALYSIS AND RESULTS

3.1. Evolution of the EUV Wave

We used base ratio images to study wave evolution. Images were first prepared and differentially rotated to the same pre-event time at 11:50 UT using the standard IDL routines in Solar Software. Then an image taken around 11:50 UT was selected as the reference image for each channel; all of these images were divided by the corresponding reference images. Figure 1 and the associated Animation 1 in the online version of the journal show the on-disk evolution of the EUV wave in EUVI-A 195 Å. The eruption site is located on the southern side of AR 11149. Due to the great magnetic gradient to the north, the EUV wave propagates mainly southward instead of isotropically. First observed at 12:00 UT, the wave front initially expands very fast. By 12:05 UT, it has been fully developed, appearing as a diffuse bright rim that covers an angular span over 110° (Figure 1(b)). Dimming regions are seen following the expanding wave front. Afterward, the bright wave front undergoes a significant deceleration, especially in the south direction, and finally stops in the southern hemisphere, forming a stationary bright stripe along the latitudinal direction (Figures 1(e) and (f)). As the bright wave front slows down, another much fainter front emanates and propagates ahead of it, attaining a distance far beyond the stationary front (Figures 1(c)–(f) and Animation 1). However, due to the relatively low cadence and sensitivity of EUVI, as well as the nature of the base ratio method, this wave signal weakens so quickly that its evolution cannot be reliably traced in EUVI-A.

In order to investigate the wave kinematics in EUVI-A in an objective manner, we adopted the semi-automated detection algorithm described in Long et al. (2011) to identify and track the bright wave front. We selected a wave sector extending from the eruption center (−100″, 300″) in the direction 180° ± 5° (directly southward), within which the wave kinematics were studied. A perturbation profile was derived by averaging the base ratio intensity values in annuli of 1° width with increasing radii on the spherical solar surface. At each observation time, the perturbation profile was fitted with a Gaussian curve, the peak

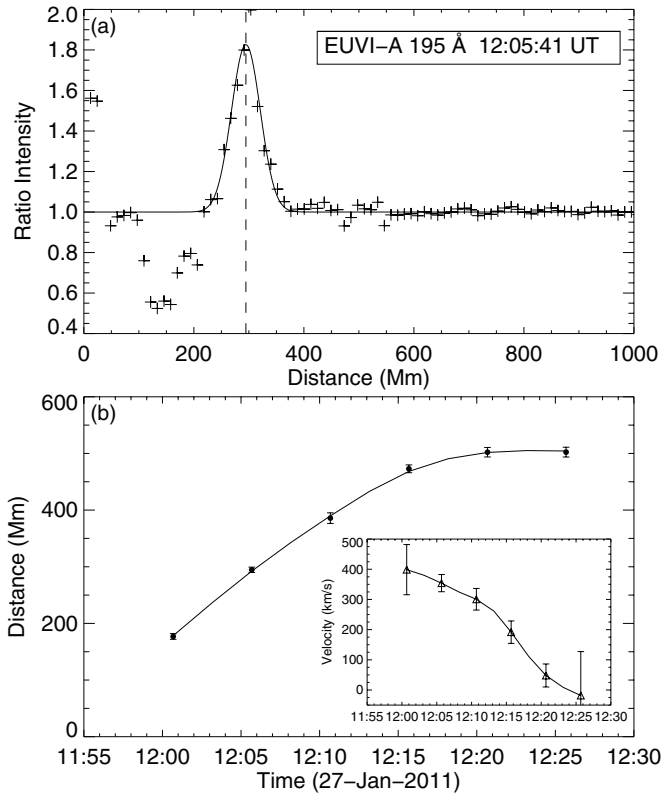

Figure 2. Top: Gaussian fit to the perturbation profile (plus signs) of the EUV wave at 12:05:41 UT except for the flaring and deep dimming sections. The vertical dashed line marks the position of the Gaussian peak that represents the distance of the wave front at that time. Bottom: time–distance diagram of the bright wave front (filled circles) together with the spline fit. Inset is the velocity evolution derived from differentiation to the fitted points (triangles) using three-point Lagrangian interpolation.

position of which was taken as the distance of the wave front. Figure 2(a) illustrates such a Gaussian fit to the perturbation profile of the EUV wave at 12:05 UT. It is worth noting that the intensity enhancement of the EUV wave at that time was as high as 80%. The distinct deceleration of the bright wave front is validated by the wave kinematics shown in Figure 2(b). The wave front decelerates from an initial speed of 398 km s^{-1} to zero velocity within a period of 20 minutes. Eventually, it turns into a stationary front at a distance ∼500 Mm south of the eruption center.

Online Animations 2–4 show the limb evolution of the EUV wave in AIA 211, 193, and 171 Å, respectively. Some snapshots of the animations are displayed in Figure 3. A front appears around 12:00 UT (Figure 3(a)), and strengthens quickly into a diffuse bright front in 211 Å and 193 Å (Figures 3(b) and (g)). However, in 171 Å, the main body of the front appears dark (Figure 3(i)). The front is largely inclined to the limb, so in the early stage it mainly propagates laterally rather than radially. Due to the extremely high cadence and sensitivity of AIA, as well as a lower background with less contribution from the disk, the emanation and separation of a secondary faint front from the primary front are revealed when the primary front encounters a large coronal loop system (clearly seen in 171 Å) and then slows down (Animations 2–4). Afterward, the two fronts evolve independently. The primary front decelerates significantly and finally stops (Figures 3(f), (h), and (i)), while the secondary front travels farther as it gradually fades out (Animations 2–4).

To avoid any ambiguities introduced from close-to-limb disk regions, we studied the off-limb wave behavior at a heliocentric height of 1.1 $R_\odot$ (the black circle in Figure 3), since there is mounting evidence that EUV waves are confined to a region 1–2 scale heights above the chromosphere (e.g., Patsourakos & Vourlidas 2009). Along the circle we actually traced the evolution of the EUV wave in nearly the same direction as that selected in EUVI-A. Figure 4 shows the time–position-angle (P.A.) diagrams of the EUV wave in AIA 211, 193, and 171 Å, respectively. It is clearly seen that the kinematics of the EUV wave are almost the same among different channels, with the red and blue lines visually tracking the primary and secondary fronts, respectively.

We converted the P.A. values to distances from the eruption center (at a P.A. of ∼282°) and then redrew the trajectories of the primary and secondary fronts in Figure 5(a). For comparison, we overplotted the time–distance data of the bright wave front in EUVI-A 195 Å, which were multiplied by a factor of 1.1 to compensate for the difference in tracing heights (1.1 $R_\odot$ for AIA versus 1.0 $R_\odot$ for EUVI-A). As expected, the kinematics of the primary front in AIA are in perfect agreement with those of the bright wave front in EUVI-A, indicating that these two fronts are the same feature but viewed from different perspectives. The velocity evolution of the primary and secondary fronts is displayed in Figure 5(b). The primary front exhibits an initial speed of 443 km s^{-1} and undergoes only a slight deceleration in the early stage. At 12:07 UT, the exact time when the primary front interacts with the large coronal loop system south of it and starts to decelerate significantly, the secondary front emanates from the primary front with a higher starting speed of 553 km s^{-1}. From that point, the separation of the two fronts continues to increase, leading to decoupling. The velocity of the primary front finally decreases to zero, and the secondary front also decelerates considerably before its strength quickly drops below the detectable level. We should bear in mind that the kinematic analysis for the secondary front is subject to many more uncertainties than that for the primary front, due to its much fainter appearance. Although we lack any quantitative comparisons, we believe that the secondary front in AIA corresponds to the very weak wave signature in EUVI-A.

As can also be seen in Figure 4, the two fronts in AIA show different emission patterns. The primary front exhibits prominent emission enhancement in 211 Å, moderate enhancement in 193 Å, but deep depletion in 171 Å. The emission reduction of the wave front in 171 Å was previously reported (e.g., Dai et al. 2010; Liu et al. 2010). For the secondary front, it is the strongest in 193 Å, relatively weaker in 211 Å, and nearly invisible in 171 Å.

3.2. Associated Phenomena

There is a *GOES* C1.2 class flare associated with the EUV wave. The *GOES* 1–8 Å soft X-ray (SXR) light curve in Figure 6(a) indicates that the flare takes place between 11:53 UT and 12:05 UT, with the peak time at 12:01 UT. During the event time, the *RHESSI* satellite was affected by the South Atlantic Anomaly. Thus, we used the derivation of the *GOES* SXR light curve shown in Figure 6(b) as a proxy of the hard X-ray (HXR) evolution of the flare. The HXR light curve so derived also peaks at around 12:01 UT, slightly earlier than the SXR peak. Both the SXR and HXR light curves indicate that this is an impulsive flare. By the peak time of the flare, the primary front has been formed over a large distance, implying that the impulsive flare pulse occurs too late to drive the EUV wave event.

Radio observations from the Radio Solar Telescope Network (RSTN; 25–180 MHz) in the period of interest are displayed

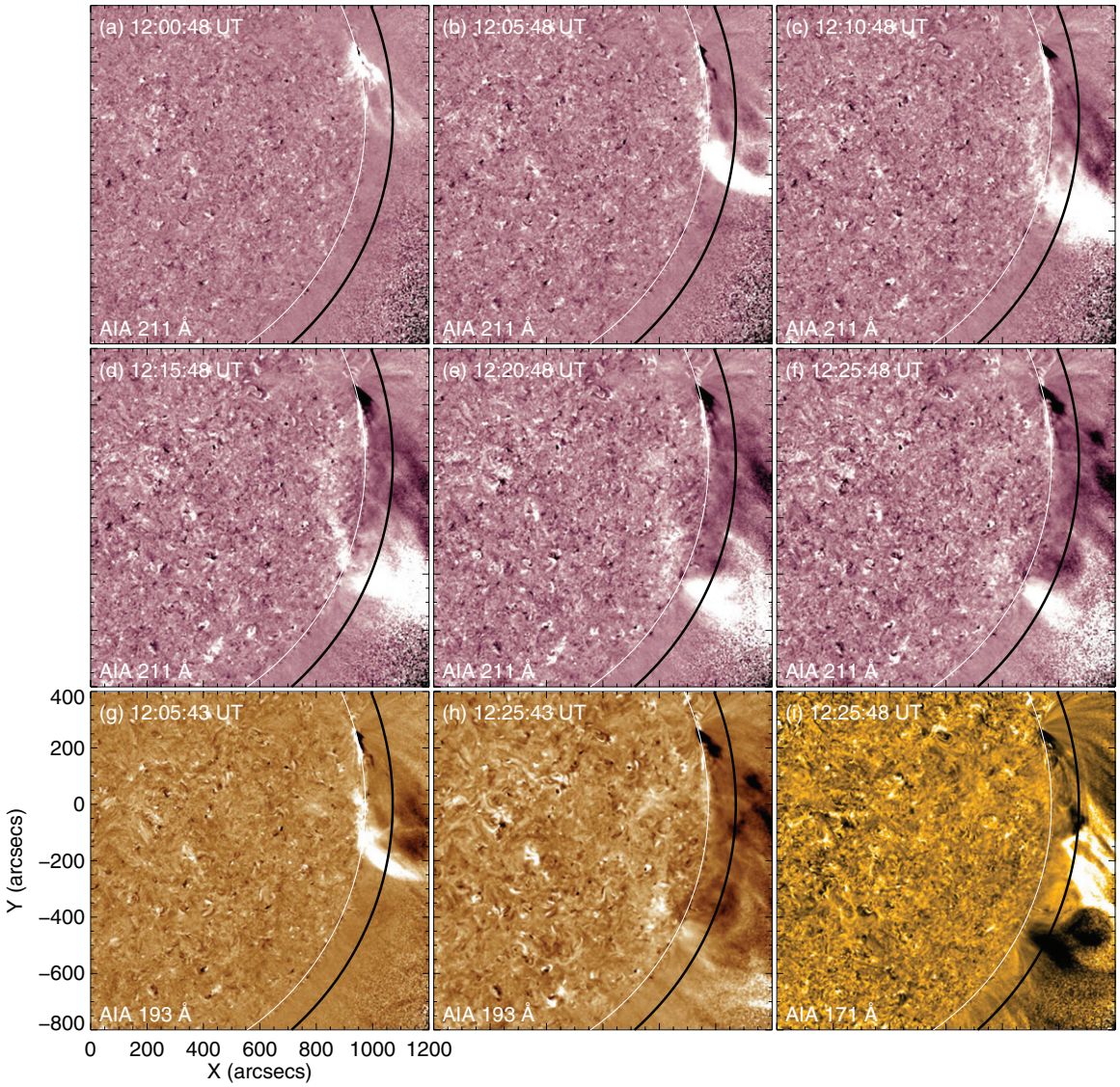

Figure 3. Base ratio snapshots of the EUV wave taken by *SDO*/AIA at 211 (a–f), 193 (g–h), and 171 Å (i), respectively. The black circle is located 0.1 $R_{\odot}$ above the limb along which the off-limb evolution of the EUV wave is traced.

(Animations and a color version of this figure are available in the online journal.)

in Figure 6(c) as a dynamic spectrum in the metric domain. Besides a type III burst that coincides with a small HXR spike at 11:59 UT, the dominant feature is a type II burst starting from 12:08 UT, with a staring frequency of 83 MHz at the harmonic band. The occurrence of the metric type II burst follows the decoupling of the primary and secondary fronts within 1 minute, which may reflect a physical link between the decoupling process and a coronal shock. However, when assuming a coronal density model for the quiet Sun at solar minimum, which was proposed by Saito et al. (1977), the coronal shock inferred from the type II burst starts at a heliocentric height over 1.4 $R_{\odot}$, significantly higher than the detectable altitude of the secondary front. In addition, the signal of the secondary front is very weak. Therefore, if the secondary front is a part of the coronal shock, it must be away from the nose of the shock.

The EUV wave also triggers transverse oscillations of a prominence over the southwestern limb. Figure 7(a) displays the prominence morphology in AIA 193 Å, which appears as a dark feature at a P.A. of 248°. We studied the prominence oscillations along the azimuthal direction (the white slice in Figure 7(a)). As shown in Figure 7(b), the transverse oscillations start from 12:10 UT, with the multiple prominence threads first moving southward and then moving northward. The oscillation period is about 14 minutes, and the maximum amplitude is about 8000 km. Compared with the wave kinematics, the start of the prominence oscillations coincides with the arrival of the secondary front, which can be further validated by the bright features at 12:10 UT in Figure 7(b). This observational factor may indicate that the secondary front has a wave nature. Recently, Asai et al. (2012) and Liu et al. (2012) also observed prominence transverse oscillations triggered by limb EUV waves. The oscillation parameters in our study are consistent with those in Asai et al. (2012). In Liu et al. (2012), the prominence oscillations last for a longer interval, with oscillation periods that are about twice as long. Nevertheless, the physics that determines the oscillation parameters is beyond the scope of this paper.

4. DISCUSSION

We report the *STEREO-A*/EUVI and *SDO*/AIA quadrature observations of the EUV wave event on 2011 January 27, in

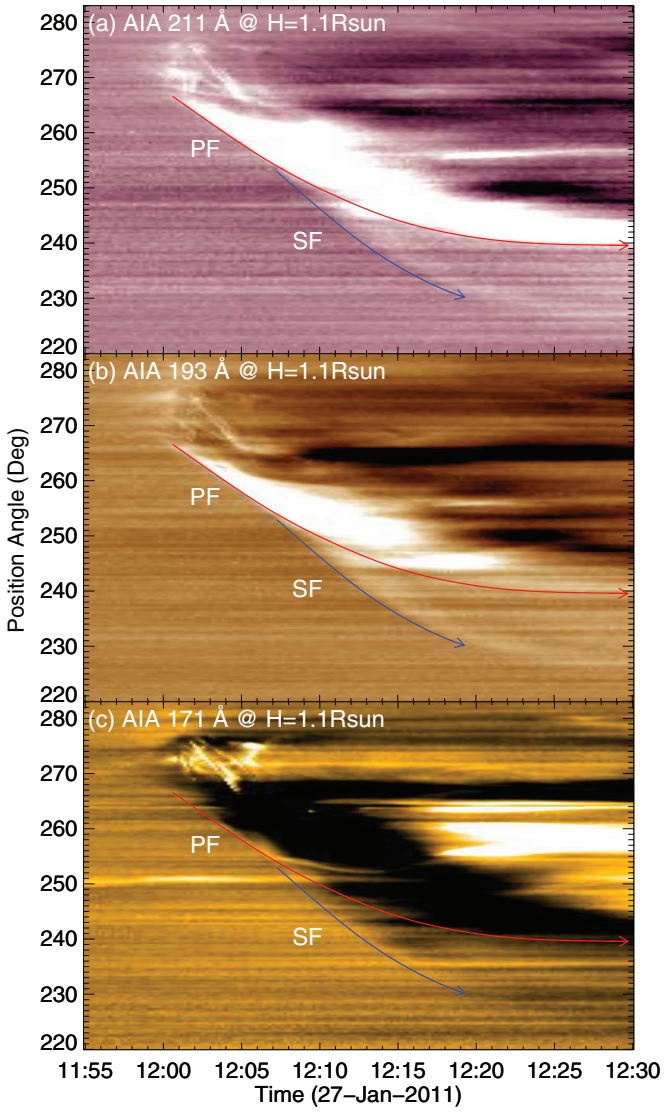

Figure 4. Time–P.A. diagrams of the EUV wave in *SDO*/AIA 211 (a), 193 (b), and 171 Å (c), respectively. The red line (PF) follows the primary front, while the blue line (SF) tracks the secondary front. The P.A. values are counted counterclockwise from solar north.

(A color version of this figure is available in the online journal.)

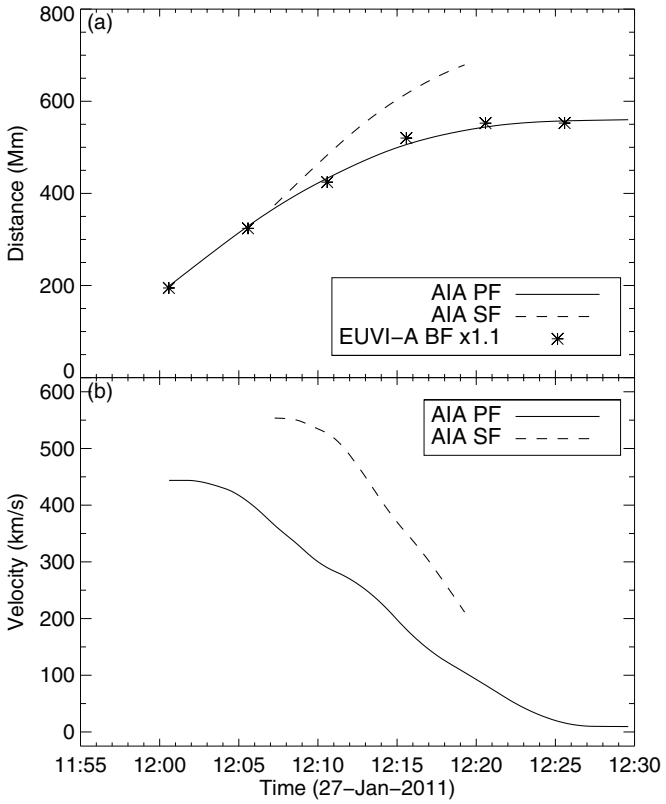

Figure 5. Top: time–distance diagram of the primary (solid line) and secondary (dashed line) fronts in AIA. The overplotted asterisks are the same time–distance data of the bright wave front in EUVI-A 195 Å in Figure 2(b) but multiplied by a factor of 1.1. Bottom: the velocity evolution of the primary (solid line) and secondary (dashed line) fronts obtained using the same method as that for the bright wave front in EUVI-A. Note that the cadence of the measurements for AIA is 12 s.

which two fronts and their decoupling are revealed. From the edge-on perspective of AIA, the wave fronts extend to quite a high altitude, implying that the kinematic analysis from the single face-on perspective of EUVI-A would somewhat underestimate the wave speed owing to a lack of knowledge about the height of the line-of-sight integration maximum (Kienreich et al. 2009). Therefore, the value of ~440 km s^{-1} measured at 0.1 $R_\odot$ above the limb may reflect the actual initial speed of the primary front more accurately. The first appearance of the primary front occurs earlier than the peak of the associated impulsive flare, which invalidates a flare driver of the EUV wave event.

The primary and secondary fronts show distinct differences in amplitude, kinematics, and multi-temperature behavior, which implies that they are due to different physical mechanisms. In Figure 8 we show the coronal magnetic topology close to the event time, which was extrapolated from the *SOHO*/Michelson Doppler Imager (MDI; Scherrer et al. 1995) synoptic magnetogram with the potential-field source-surface (PFSS; Schrijver & De Rosa 2003) model. The extrapolated magnetic field lines are overlaid on the simultaneous base ratio images of the EUV wave in AIA 193 Å and EUVI-A 195 Å at 12:25 UT when the primary front has turned into a stationary front. The magnetic topology shows a large-scale magnetic system that covers an extent from AR 11149 to the elongated magnetic separatrix on the southern hemisphere. It is clearly seen that the stationary front is indeed cospatial with the magnetic separatrix, indicative of the non-wave nature of the primary front. By contrast, the secondary front triggers transverse oscillations of a prominence and travels across the magnetic separatrix to a farther distance, which is a typical characteristic of fast-mode waves.

As seen from the AIA limb observations, the primary front extends continuously down to the limb, which might not be explained by the current shell model (Delannée 2000), in which the brightening due to Joule heating is confined quite high in the corona. The lack of a detailed small-scale magnetic topology makes us unable to judge if the successive reconnection model (Attrill et al. 2007) works for this event. Instead, the field-line stretching mode (Chen et al. 2002, 2005) seems to be a reasonable explanation. In this model, the primary front corresponds to the CME frontal loop that is composed of the newly stretched magnetic field lines. Guided by the overlying large-scale magnetic system, in the early stage the CME frontal loop propagates with a substantial inclination toward the limb, showing a fast lateral expansion. Meanwhile, a large amount of material is quickly piled onto the frontal loop, resulting in a nonlinear density enhancement (Figure 2(a), assuming a wide temperature

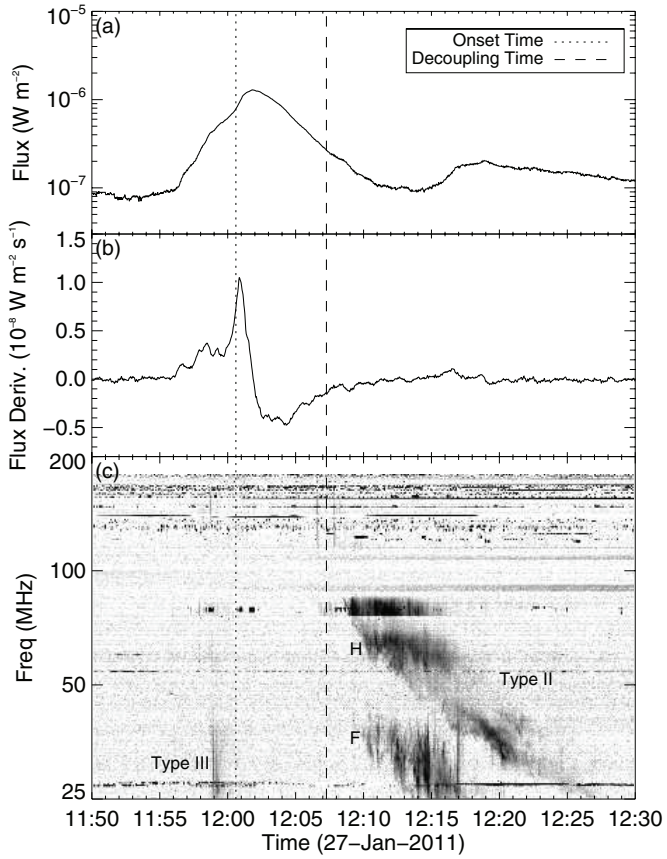

Figure 6. X-ray and radio observations of the event. The top two panels show the *GOES* 1–8 Å light curve (a) and its derivation smoothed by a boxcar of 30 s (b), respectively. The bottom panel shows the radio dynamic spectrum obtained by RSTN (25–180 MHz), in which a type III burst and a type II burst are revealed. The letter "F" ("H") denotes the fundamental (harmonic) band of the type II burst. The vertical dotted line indicates the onset time of the EUV wave, and the vertical dashed line represents the decoupling time of the primary and secondary fronts.

coverage of the EUVI 195 Å channel). Furthermore, this adiabatic compression process leads to considerable heating. The heating effect makes further positive contributions to the emission enhancement in the hotter AIA 211 Å channel (with T_{peak} of ∼2 MK) in addition to the density enhancement (Figure 4(a)). In the AIA 193 Å channel (T_{peak} ∼ 1.3 MK, a typical coronal temperature), such contributions may not be so significant, or could even be somewhat negative (Figure 4(b)). For the cooler AIA 171 Å channel (T_{peak} of ∼0.6 MK), the response function decreases very fast from the peak with increasing temperatures. Therefore, in 171 Å, the heating strongly reduces the emission (Figure 4(c)), and the density enhancement cannot compensate for the emission decrease caused by the temperature rise. According to the field-line stretching model, the CME can only stretch the magnetic field lines of the same magnetic system within which the CME is involved. At the magnetic separatrix, a border with other magnetic systems, the CME frontal loop stops and forms a stationary front. It is worth noting that an associated CME is later observed in the high corona (see http://spaceweather.gmu.edu/seeds/lasco.php), whose southern border is roughly located at the P.A. of the magnetic separatrix.

It is believed that the CME has driven a fast-mode wave since it started the lateral expansion. However, this fast-mode wave is not distinguishable from the CME until the CME frontal loop encounters the large coronal loop system south of it. The interaction between the CME and the coronal loop system not only slows down the CME lateral expansion but also increases the local fast-mode speed. As a result, the fast-mode wave (the secondary front) emanates from the CME frontal loop with a relatively higher "starting" speed (∼550 km s^{-1}). From that point, the fast-mode wave is decoupled from the CME and the two components evolve independently. The CME's propagation changes from mainly in the lateral direction to mainly in the radial direction. As the CME propagates radially outward, the Alfvén speed first increases to a maximum and then decreases, facilitating the formation of a CME-driven shock at a relatively high altitude. This could be a reasonable explanation for the metric type II burst in this work. We note that the case study of a coronal shock by Gopalswamy et al. (2012) shows that the Alfvén speed attains a maximum of ∼450 km s^{-1} at a heliocentric height of ∼1.35 $R_\odot$. For the fast-mode wave, it travels across the magnetic field lines freely, and triggers the prominence transverse oscillations over the southwestern limb. As the fast-mode wave propagates into quiet-Sun regions, the decrease in the magnetic strength leads to wave deceleration. Compared to the CME frontal loop, the fast-mode wave is much fainter. In addition, the wave signature is stronger in 193 Å than in 211 Å, and almost invisible in 171 Å. Combining these

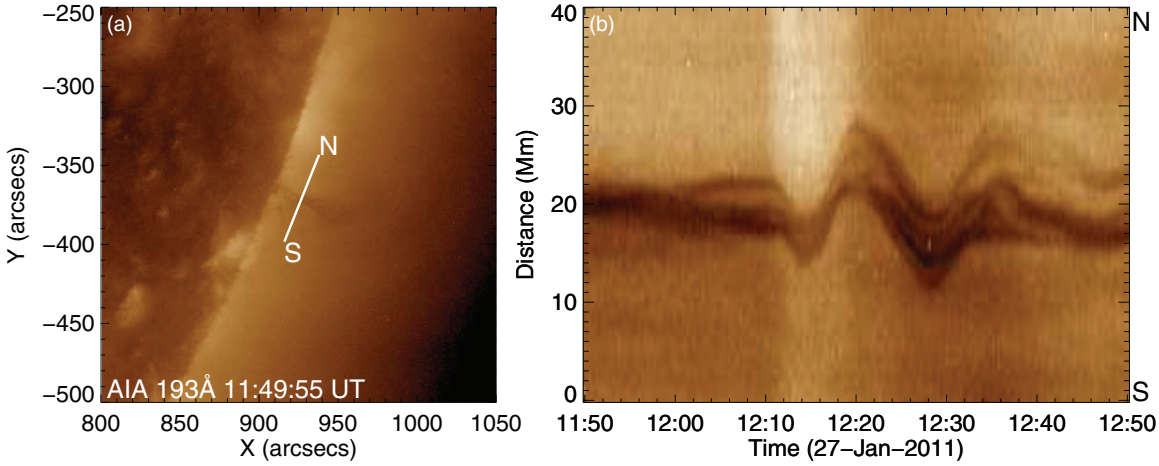

Figure 7. Left: pre-event AIA 193 Å image showing a prominence at a P.A. of 248°. Right: time–distance diagram of the oscillating prominence along the white slice outlined in the left panel. The distances are measured from the south.

(A color version of this figure is available in the online journal.)

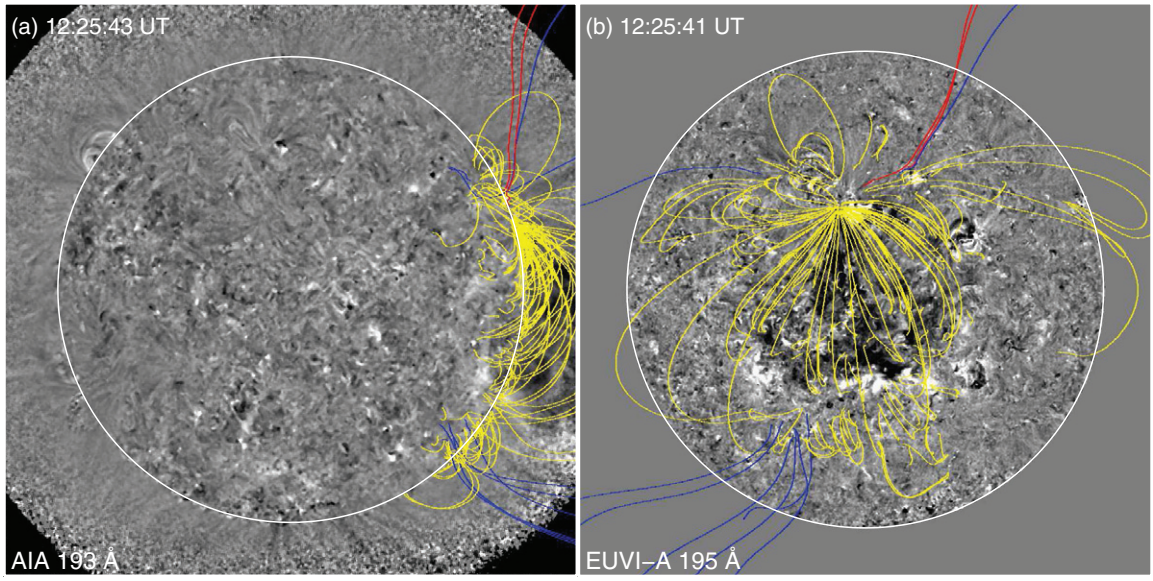

Figure 8. Coronal magnetic topology close to the event time, which is extrapolated from the *SOHO*/MDI data with the PFSS model, overlaid on the simultaneous base ratio images of the EUV wave in *SDO*/AIA 193 Å (left) and *STEREO-A*/EUVI-A 195 Å (right) according to each spacecraft's perspective. The yellow lines represent closed magnetic field lines, and the blue (red) lines denote open magnetic field lines from positive (negative) polarity.

(A color version of this figure is available in the online journal.)

observational facts, we suggest that the fast-mode wave is a linear MHD wave that propagates through a medium of the typical coronal temperature.

As mentioned above, there have been several observational studies dealing with EUV wave events with two fronts and their decoupling. Cheng et al. (2012) found that the lateral expansion of the CME bubble first accelerates and the diffuse front is separated from the CME bubble shortly after the lateral expansion slows down. In their case, the associated flare is rather gradual, and the acceleration of the CME coincides with the flare's rising phase. In our study, the associated flare is an impulsive one, so the CME may undergo a very impulsive acceleration in its initiation phase (cf. Zhang et al. 2001). As a result, upon its first appearance, the CME lateral expansion (primary front) has already attained a maximum speed of $\sim$440 km s^{-1}. Furthermore, the lateral expansion of the CME bubble in Cheng et al. (2012) should reflect an intrinsic expansion of the CME, while in our case the CME lateral expansion is mainly guided by the overlying large-scale magnetic system. The event studied by Asai et al. (2012) is a very intense one, in which an Hα Moreton wave is observed cospatially with the sharp, bright EUV wave front appearing in the very early stage. This implies that at the very beginning, the major CME has driven a coronal MHD wave that was initially strong enough to penetrate the chromosphere, which is further validated by a concurrent metric type II burst. As the bright EUV wave front (which we believe corresponds to the CME frontal loop) decelerates to an "ordinary EIT wave," the MHD wave is detached from the CME and its strength decreases to the linear regime—unable to perturb the chromosphere any more. However, in our study, the secondary front keeps a linear MHD wave during its whole evolution process. If the secondary front is a part of the coronal shock that starts shortly after the decoupling of the two fronts, it must be away from the nose of the shock where the wave strength is the strongest. Chen & Wu (2011) also observed that the slow wave front finally stops at a magnetic separatrix. The event they studied is associated with a microflare, and no CMEs are detected during the event time. In our study, an associated CME is observed later, with the location of its southern border consistent with the P.A. of the magnetic separatrix. This supplies further evidence for the non-wave nature of the primary front.

Finally, we note that the EUV wave is the second of three homologous EUV wave events studied in Kienreich et al. (2012). They found that the wave is later reflected at the border of the extended coronal hole at the southern polar region. Hence, they concluded that the EUV wave is purely a fast-mode wave. We maintain that the reflected wave should correspond to the secondary front in our study, which is indeed a fast-mode wave. In the early stage, it is actually attached to the non-wave CME component.

5. CONCLUSIONS

By using the *STEREO-A*/EUVI and *SDO*/AIA quadrature observations of an EUV wave event on 2011 January 27, two fronts and their decoupling are revealed. The two fronts show distinct differences in amplitude, kinematics, and multi-temperature behavior. Complementary X-ray and radio observations lead us to the conclusion that the two fronts are of different natures. The primary front belongs to a non wave CME component, which can be reasonably explained with the field-line stretching model. As for the secondary front, it is most likely a linear fast-mode MHD wave that propagates through a medium of the typical coronal temperature. The decoupling of the two fronts is caused by the interaction of the CME frontal loop and a large coronal loop system south of it.

We are grateful to the anonymous referee whose constructive comments led to a significant improvement of the manuscript. This work is supported by NSFC under grants 11103009, 10933003, 11078004, and 11025314, and by NKBRSFC under grant 2011CB811402. Y.D. is also sponsored by SRFROCS, Ministry of Education. We thank the *STEREO*/SECCHI, *SDO*/AIA, *GOES*, and RSTN consortia for their open data policy.

REFERENCES

Asai, A., Ishii, T. T., Isobe, H., et al. 2012, ApJ, 745, L18
Attrill, G. D. R., Engell, A. J., Wills-Davey, M. J., Grigis, P., & Testa, P. 2009, ApJ, 704, 1296
Attrill, G. D. R., Harra, L. K., van Driel-Gesztelyi, L., & Démoulin, P. 2007, ApJ, 656, L101
Cheng, X., Zhang, J., Olmedo, O., et al. 2012, ApJ, 745, L5
Chen, P. F. 2009, ApJ, 698, L112
Chen, P. F. 2011, Living Rev. Sol. Phys., 8, 1
Chen, P. F., Fang, C., & Shibata, K. 2005, ApJ, 622, 1202
Chen, P. F., Wu, S. T., Shibata, K., & Fang, C. 2002, ApJ, 572, L99
Chen, P. F., & Wu, Y. 2011, ApJ, 732, L20
Cohen, O., Attrill, G. D. R., Manchester, W. B., IV, & Wills-Davey, M. J. 2009, ApJ, 705, 587
Dai, Y., Auchère, F., Vial, J.-C., Tang, Y. H., & Zong, W. G. 2010, ApJ, 708, 913
Delaboudinière, J.-P., Artzner, G. E., Brunaud, J., et al. 1995, Sol. Phys., 162, 291
Delannée, C. 2000, ApJ, 545, 512
Delannée, C., & Aulanier, G. 1999, Sol. Phys., 190, 107
Downs, C., Roussev, I. I., van der Holst, B., Lugaz, N., & Sokolov, I. V. 2012, ApJ, 750, 134
Downs, C., Roussev, I. I., van der Holst, B., et al. 2011, ApJ, 728, 2
Gallagher, P. T., & Long, D. M. 2011, Space Sci. Rev., 158, 365
Gopalswamy, N., Nitta, N., Akiyama, S., Mäkelä, P., & Yashiro, S. 2012, ApJ, 744, 72
Gopalswamy, N., Yashiro, S., Temmer, M., et al. 2009, ApJ, 691, L123
Harra, L. K., & Sterling, A. C. 2003, ApJ, 587, 429
Howard, R. A., Moses, J. D., Vourlidas, A., et al. 2008, Space Sci. Rev., 136, 67
Kaiser, M. L., Kucera, T. A., Davila, J. M., et al. 2008, Space Sci. Rev., 136, 5
Kienreich, I. W., Muhr, N., Veronig, A., et al. 2012, Sol. Phys., in press (arXiv:1204.6472)
Kienreich, I. W., Temmer, M., & Veronig, A. M. 2009, ApJ, 703, L118
Lemen, J. R., Title, A. M., Akin, D. J., et al. 2012, Sol. Phys., 275, 17
Li, T., Zhang, J., Yang, S., & Liu, W. 2012, ApJ, 746, 13
Liu, W., Nitta, N. V., Schrijver, C. J., Title, A. M., & Tarbell, T. D. 2010, ApJ, 723, L53
Liu, W., Ofman, L., Nitta, N. V., et al. 2012, ApJ, 753, 52
Long, D. M., Gallagher, P. T., McAteer, R. T. J., & Bloomfield, D. S. 2008, ApJ, 680, L81
Long, D. M., Gallagher, P. T., McAteer, R. T. J., & Bloomfield, D. S. 2011, A&A, 531, A42
Moses, D., Clette, F., Delaboudinière, J.-P., et al. 1997, Sol. Phys., 175, 571
Patsourakos, S., & Vourlidas, A. 2009, ApJ, 700, L182
Patsourakos, S., & Vourlidas, A. 2012, Sol. Phys., in press (arXiv:1203.1135)
Patsourakos, S., Vourlidas, A., Wang, Y. M., Stenborg, G., & Thernisien, A. 2009, Sol. Phys., 259, 49
Pesnell, W. D., Thompson, B. J., & Chamberlin, P. C. 2012, Sol. Phys., 275, 3
Saito, K., Poland, A. I., & Munro, R. H. 1977, Sol. Phys., 55, 121
Scherrer, P. H., Bogart, R. S., Bush, R. I., et al. 1995, Sol. Phys., 162, 129
Schrijver, C. J., & De Rosa, M. L. 2003, Sol. Phys., 212, 165
Thompson, B. J., Gurman, J. B., Neupert, W. M., et al. 1999, ApJ, 517, L151
Thompson, B. J., Plunkett, S. P., Gurman, J. B., et al. 1998, Geophys. Res. Lett., 25, 2465
Uchida, Y. 1968, Sol. Phys., 4, 30
Veronig, A. M., Temmer, M., & Vršnak, B. 2008, ApJ, 681, L113
Veronig, A. M., Temmer, M., Vršnak, B., & Thalmann, J. K. 2006, ApJ, 647, 1466
Wang, H., Shen, C., & Lin, J. 2009, ApJ, 700, 1716
Wang, Y.-M. 2000, ApJ, 543, L89
Warmuth, A., Vršnak, B., Magdalenić, J., Hanslmeier, A., & Otruba, W. 2004, A&A, 418, 1117
Wills-Davey, M. J., & Attrill, G. D. R. 2009, Space Sci. Rev., 149, 325
Wills-Davey, M. J., DeForest, C. E., & Stenflo, J. O. 2007, ApJ, 664, 556
Wuelser, J.-P., Lemen, J. R., Tarbell, T. D., et al. 2004, Proc. SPIE, 5171, 111
Wu, S. T., Zheng, H., Wang, S., et al. 2001, J. Geophys. Res., 106, 25089
Zhang, J., Dere, K. P., Howard, R. A., Kundu, M. R., & White, S. M. 2001, ApJ, 559, 452
Zhukov, A. N. 2011, J. Atmos. Sol.-Terr. Phys., 73, 1096
Zhukov, A. N., & Auchère, F. 2004, A&A, 427, 705